reinforced concrete curb of a masonry building in the study area (3.52A).

To track potentially unstable blocks or sectors of the rock walls, rounded optical prisms were installed on both rock surfaces and nearby structures. The choice of prism type was determined by the distance from the reference base: microprisms were used for distances shorter than 200 m, whereas macroprisms were employed for longer ranges (Figure 3.52C).

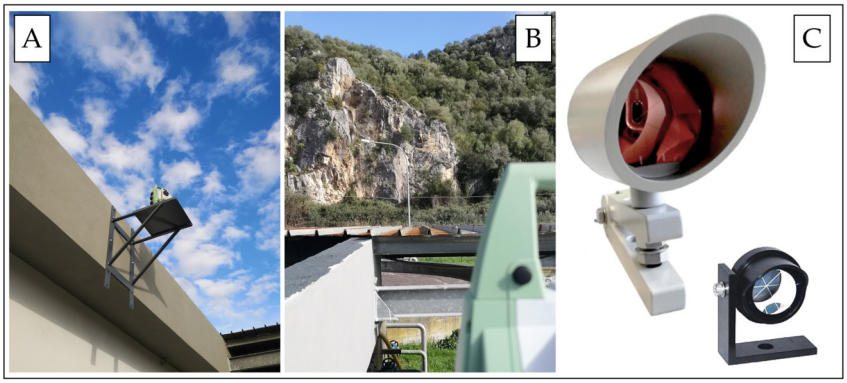

Figure 3.52: Panel (A) shows the Robotic Total Station (RTS) mounted on a steel plate anchored to a reinforced concrete curb. Panel (B) presents the rock walls observed from the RTS station, while panel (C) depicts the macroprism and microprism employed during the multitemporal RTS monitoring campaigns.

The distinction between the two lies in the reflective crystal diameter—25.4 mm for microprisms and 63 mm for macroprisms—and in their measurement precision, which is better than 3″ and 5″, respectively.

On the basis of the engineering–geological survey and the outcomes of the kinematic stability analysis, a total of 34 prisms were installed (Figure 3.53). Among them, 30 were designated as monitoring prisms (B1, B2, . . . , B30) and positioned directly on the rock walls by professional climbers. The remaining four were employed as reference prisms: three were fixed on buildings in proximity to the survey "base" (R1, R2, and R3), while one (R4) was anchored to a rock outcrop at the foot of the monitored slope, in a remote area accessible only to expert hikers or climbers.

The reference prisms were arranged to ensure a consistent RTS orientation across all surveys, thereby allowing the detection and evaluation of errors associated with each

positioning phase.

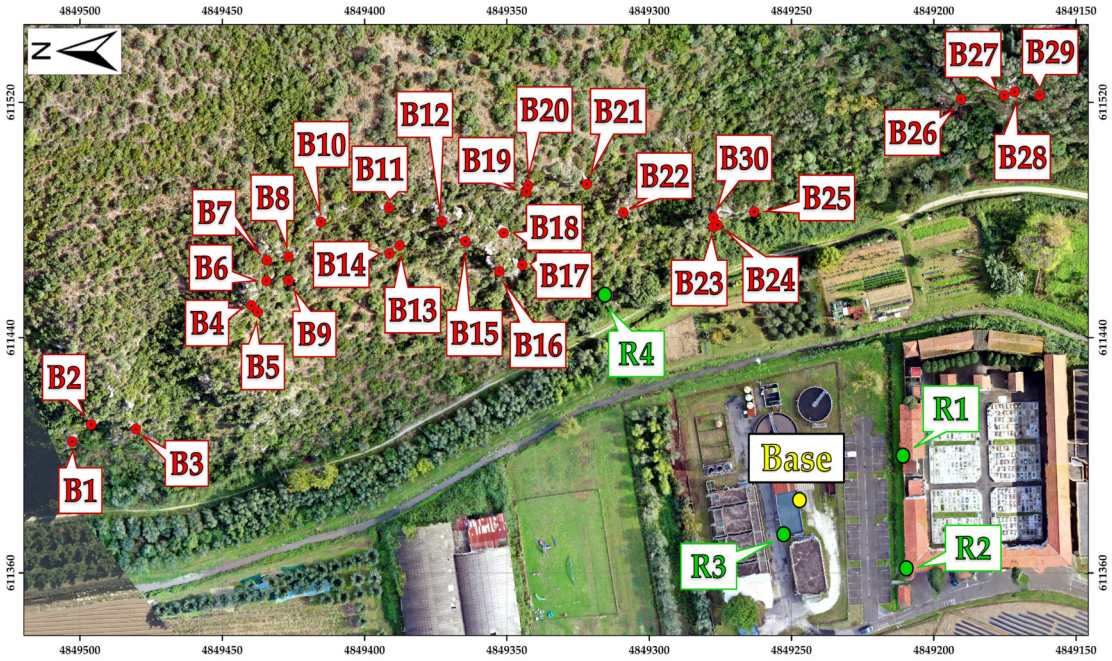

Figure 3.53: The RTS base is marked in yellow together with the distribution of the prisms. The green symbols correspond to the reference prisms adopted to orient the monitoring setup, whereas the red ones represent the monitoring prisms repeatedly measured throughout the nine multitemporal survey sessions.

During each survey, the RTS was configured to acquire 10 double-sided measurements for every prism, and the mean value was then computed. This procedure, also referred to as the "two-faces" measurement, involves first observing the prism with the normal face of the instrument and subsequently with the opposite face. By averaging the results obtained from both orientations, part of the instrumental error is compensated. This approach was adopted to improve the overall accuracy and reliability of the dataset, as it reduces noise and interference, corrects for systematic errors, identifies anomalies due to temporary obstructions, and increases statistical robustness.

The precision of the measurements was verified after each survey, with the outcomes presented in Section 3.3.4.5.

Before data processing, the instrumental uncertainties associated with the RTS and the

prisms, together with additional possible error sources, were evaluated. This evaluation included the definition of uncertainty thresholds, below which no conclusive interpretation could be drawn.

The first element examined was the intrinsic instrumental accuracy of the RTS (as mentioned in Section 3.3.3.1). Given that the manufacturer's specified precision is 1″ for angular observations and ±1 mm (+1.5 ppm) for distance measurements, the theoretical uncertainty varies depending on both the measurement type and the distance between the RTS and the targets. Consequently, an error ellipse was defined for each monitored point. The orientation of the ellipse is such that the major axis lies orthogonal to the line of sight between the RTS and the prism, while the minor axis is parallel to it, with dimensions depending on the prism's distance from the reference base (Table 3.22).

Angular uncertainty (Δd_θ) was calculated according to the following relation:

$$\Delta d_\theta(\pm\text{mm}) = \tan\left(\frac{1}{3600}\right) \times D \tag{3.5}$$

where D is the distance between prism and RTS.

Distance uncertainty (Δd) was defined as:

$$\Delta d(\pm\text{mm}) = 1 + \left(1.5 \times \frac{D}{1{,}000{,}000}\right) \tag{3.6}$$

Since prism contributions are difficult to model rigorously due to variable atmospheric conditions and near-infrared signal delays, a precautionary additional uncertainty of ±1.5 mm was assigned to both angular and distance measurements. Other environmental factors—such as humidity, pressure, temperature fluctuations, and thermal expansion of materials—were also considered, together with potential accidental errors of various origins. While repeated measurements can reduce random errors, some contributions remain difficult to quantify and cannot be entirely eliminated.

For each survey, every prism was observed in 10 consecutive cycles using the two-

faces configuration, and the resulting values were averaged. Assuming no movement occurred between the first and last reading of a session (maximum duration ≈ 60 min), the measurement set allowed a direct computation of the standard deviation, providing a realistic estimate of uncertainty for that survey and for each individual prism. These uncertainty values—rounded up because sub-millimetric figures have no practical topographic significance—capture both instrumental and environmental contributions related to the installation context (alluvial plain of the Serchio River) and to the adopted strategy (multitemporal surveys rather than continuous monitoring). When the empirical standard deviation was smaller than the nominal instrumental uncertainty, the latter was conservatively adopted as the reference.

Table 3.22 reports the final uncertainty thresholds that combine RTS and prism specifications with the environmental component.

Table 3.22: Summary of the final uncertainty threshold values for each monitoring prism.

Prism ID	**RTS–prism distance (m)**	**Distance uncertainty (±mm)**	**Azimuthal uncertainty (±mm)**	**Elevation uncertainty (±mm)**
B1	257	3	7	4
B2	252	3	8	3
B3	235	3	6	3
B4	212	3	7	3
B5	207	3	4	3
B6	209	3	4	3
B7	213	3	4	3
B8	207	3	5	3
B9	200	3	5	3
B10	203	3	5	3
B11	186	3	3	3

continued on next page

Table 3.22 — *continued from previous page*

Prism ID	**RTS–prism distance (m)**	**Distance uncertainty (±mm)**	**Azimuthal uncertainty (±mm)**	**Elevation uncertainty (±mm)**
B12	167	3	3	3
B13	171	3	5	3
B14	172	3	4	3
B15	153	3	4	3
B16	133	3	4	3
B17	128	3	3	3
B18	143	3	5	3
B19	149	3	3	3
B20	152	3	5	3
B21	135	3	3	3
B22	119	3	4	3
B23	98	3	3	2
B24	99	3	4	2
B25	100	3	5	2
B26	149	3	6	3
B27	159	3	5	3
B28	164	3	7	3
B29	167	3	7	3
B30	103	3	5	2

As an example, Figure 3.54 illustrates the planimetric error ellipse for prism B4 produced in the GIS environment.

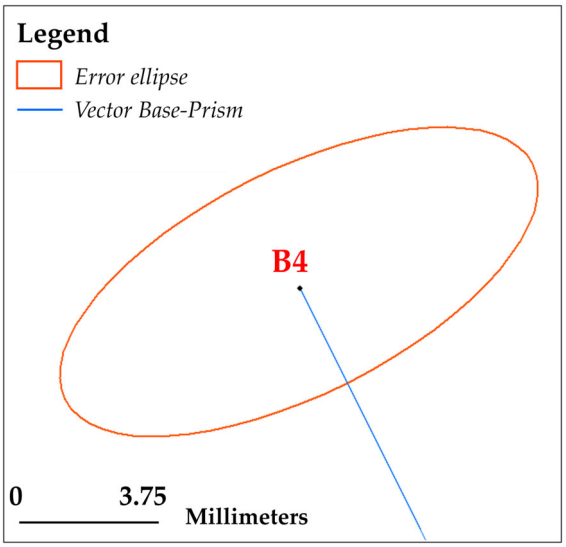

Figure 3.54: Example of error ellipse for the B4 monitoring prism.

According to this procedure, the planimetric and vertical components of uncertainty were evaluated independently. This approach makes it possible to detect potential displacement trends of the prisms, even when the observed variations remain within the limits of the error ellipse, thereby enabling the timely adoption of precautionary measures to mitigate possible rockfall events. Conversely, when a prism remains stable, the apparent positive and negative deviations are randomly distributed around the reference value of Survey n.0, and no corrective actions are required.

3.3.3.6 Persistent Scatterer Interferometry

The interferometric survey was performed to evaluate the stability of the slope crests in zones not visible from the RTS. Conventional Differential Interferometric Synthetic Aperture Radar (DInSAR) techniques work by comparing radar acquisitions from different dates, extracting millimetric ground displacements through the analysis of phase differences between signals. However, DInSAR is subject to limitations when deformation occurs at non-linear rates or when long temporal baselines are considered, since these conditions often lead to phase decorrelation (**Crosetto et al., 2016**).

To overcome such drawbacks and to characterize non-linear strain behaviors over extended periods, advanced interferometric approaches have been developed that exploit large archives of radar images and their relative phase histories. Among them, Persistent Scatterer Interferometry (PSI) focuses on the amplitude and phase stability of individual pixels—referred to as Persistent Scatterers (PSs)—which are identified by their consistently high backscattering stability over time (**Crosetto et al., 2016**). PSs may correspond to anthropogenic features, such as buildings or metallic structures, or to natural reflectors like rocky outcrops and bare ground surfaces.

In this case study, three artificial corner reflectors were designed and installed to act as PSs (Figure 3.55), following established guidelines (**Garthwaite et al., 2015**).

Figure 3.55: Metallic corner reflectors positioned along the upper edge above the rock walls: (A) map of reflector locations in the study area; photographs CR1, CR2, and CR3 illustrate detailed views of the installed devices.

Their placement was planned along the upper edge of the cliff, in areas free of vegetation, with orientations aligned to the satellite line-of-sight. The aim of this installation was to enable the detection of possible displacements occurring at the slope crest, complementing the measurements obtained with the RTS.

Over the years, numerous algorithms have been developed to implement the PSI methodology. For this study, we employed the algorithm originally proposed by **Hooper et al. (2004)**, which generates interferograms by combining a single reference acquisition with multiple secondary scenes, analyzing their relative phase differences over time. One of the strengths of this approach, compared to other PSI methods, is its ability to incorporate low-amplitude natural scatterers without assuming a predefined deformation model.

To manage and process the large datasets required for long-term monitoring, **Foumelis et al. (2018)** introduced an integrated workflow that combines the European Space Agency's SNAP (Version 7; **European Space Agency, 2022**) toolbox with the StaMPS algorithm developed by **Hooper (2008)**. This SNAP–StaMPS chain has become a standard for PSI analysis. Within this framework, candidate PSs are first identified by computing the Amplitude Dispersion Index (ADI) for each pixel. Subsequently, the temporal stability of the phase is evaluated to confirm whether a pixel qualifies as a scatterer.

The resulting PS density is strongly influenced by land cover and topographic setting. High densities are typically found in urban or anthropized contexts, where artificial features provide strong radar backscatter, whereas vegetated or agricultural areas often yield very low densities (**Fárová et al., 2019**; **Scaioni et al., 2014**; **Zhao et al., 2012**).

For the present case study, Sentinel-1A and -1B datasets were retrieved from the Alaska Satellite Facility (ASF) Data Search platform (`https://search.asf.alaska.edu/#/`). The selected acquisitions correspond to ascending orbits, in Single Look Complex (SLC) format, using the Interferometric Wide (IW) swath mode and dual polarization (VV + VH). Figure 3.56A illustrates the distribution of the images covering the area of interest, while Figure 3.56B provides an example of two scenes chosen for their spatial alignment.

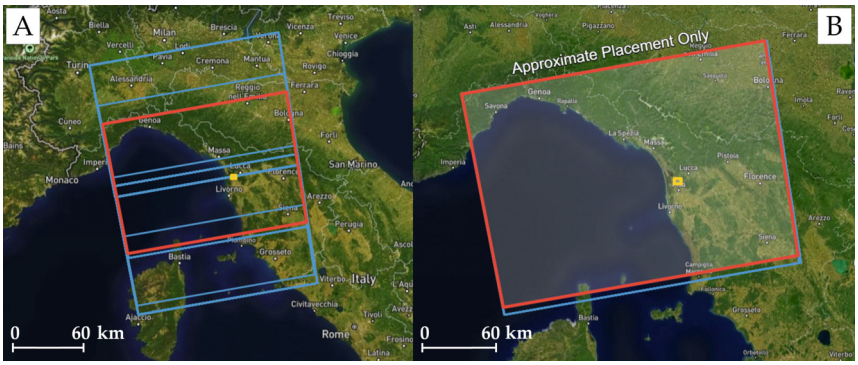

Figure 3.56: (A) Strip of satellite images of the study area; (B) corresponding satellite view of the same extent. The yellow squares highlight the area of interest.

When acquisitions show excessive spatial offsets, the analysis terminates prematurely. Conversely, high spatial and temporal coherence between images from the same path and frame ensures a reliable PSI outcome. For this reason, descending orbit datasets were discarded, as their geometric correspondence did not meet the requirements for successful analysis.

Table 3.23 provides a summary of the SAR datasets used for the interferometric analysis, including the satellite platform, the temporal coverage (first and last acquisition dates), the acquisition orbit, path and frame numbers, and the total number of processed images.

Table 3.23: Information on the SAR data utilized in the PSI analysis.

Satellite	**First and Last Scene Date**	**Acquisition Orbit**	**Path nr.**	**Frame nr.**	**Utilized Images**
Sentinel-1A	30 July 2020 – 21 January 2022	Ascending	15	139	44
Sentinel-1B	5 August 2020 – 22 December 2021	Ascending	15	137	37

3.3.4 Results

3.3.4.1 UAS photogrammetry

The UAS-based photogrammetric surveys produced a high-resolution dataset, processed with Agisoft^{TM} Metashape software (Version 2; **Agisoft LLC, 2023**). A total of

3.4 million tie points were identified and aligned, together with Ground Control Points (GCPs) and Check Points (CPs). The overall Root Mean Square Error (RMSE) obtained during processing was 9.84 cm for GCPs and 8.50 cm for CPs, confirming the reliability of the georeferencing procedure.

From the aligned images, a global 3D point cloud consisting of approximately 114 million points was generated. To optimize the analysis, the cloud was downsampled to 80 million points, focusing exclusively on the morphologies of the areas of interest (Figure 3.57A). Subsequently, a Digital Dense Elevation Model (DDEM) was interpolated from the point cloud, and a nadiral orthophotomosaic with a Ground Sampling Distance (GSD) of 5 cm/pixel was produced (Figure 3.57B).

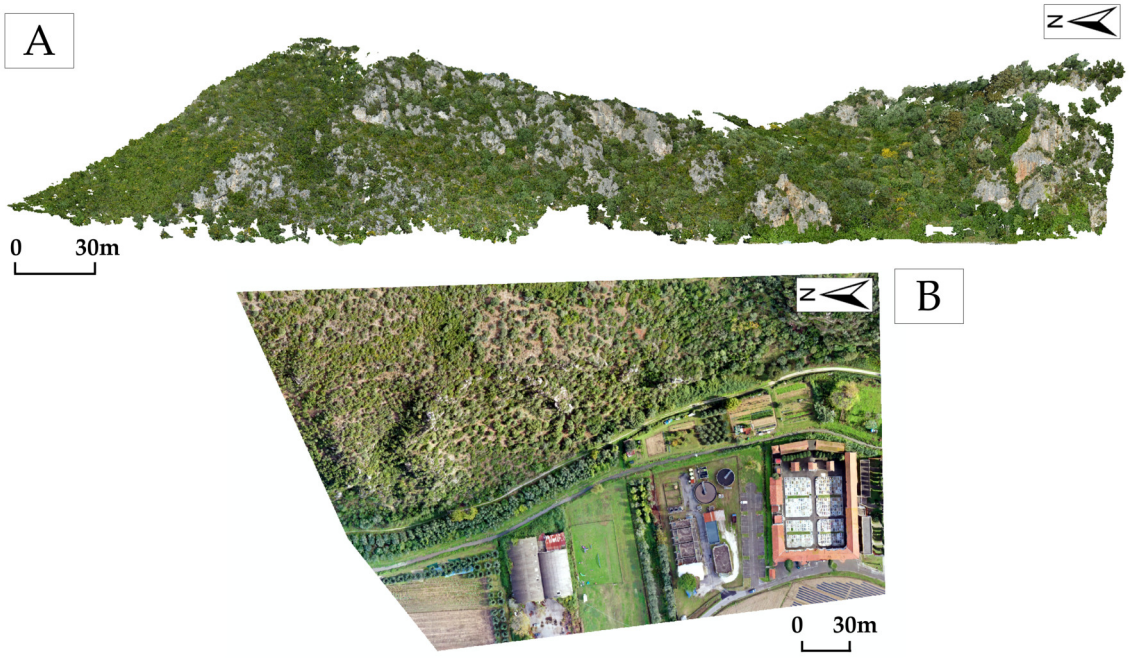

Figure 3.57: (A) Perspective view of the scaled and georeferenced 3D point cloud of the rock walls (scale bar valid for A only); (B) georeferenced orthophotomosaic of the rock walls and adjacent alluvial plain.

All outputs were georeferenced to the ETRF2000/UTM32N reference system, ensuring consistency with other survey datasets and enabling repeatability in future surveys. The availability of such georeferenced products is crucial, as it supports temporal com-

parisons, change detection, and integration with monitoring datasets. Furthermore, both the DDEM and the orthophotomosaic were very useful in mapping unstable rocky blocks and discontinuities, and in guiding the strategic installation of monitoring prisms.

3.3.4.2 Engineering–geological survey

The in situ engineering–geological survey, combined with the photointerpretation performed on the global 3D point cloud, the DDEM, and the orthophotomosaic, resulted in a joint database comprising 237 joints orientation measurements.

To assess the accuracy and reliability of the two survey approaches, the datasets were first compared using stereonet plots. Figure 3.58 presents the analysis of the 81 field measurements collected on safe and accessible outcrops at the base of the rocky walls (see also Figure 3.51), while Figure 3.59 displays the analysis of the 156 joint measurements derived from the photointerpretation of the 3D point cloud.

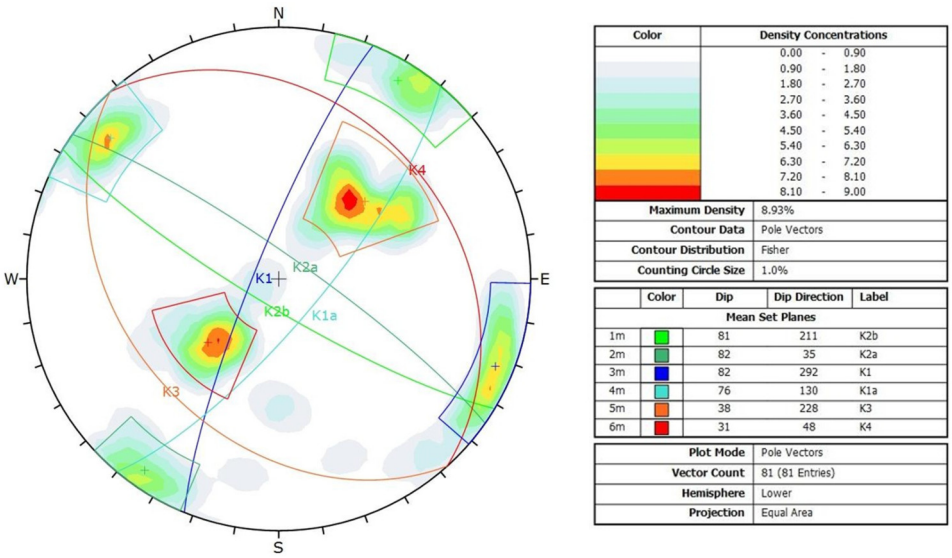

Figure 3.58: Stereographic projection (Schmidt equal-area method—lower hemisphere) of data collected during the in situ engineering–geological survey.

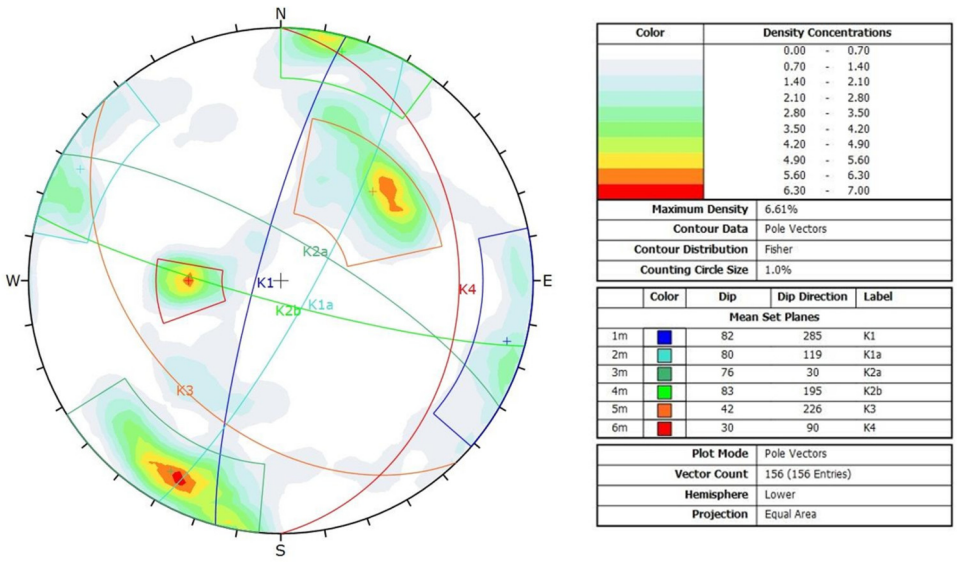

Figure 3.59: Stereographic projection (Schmidt equal-area method—lower hemisphere) of data interpreted on the 3D point cloud.

The stereonet plots highlight the overall consistency between the two datasets. The mean differences in dip and dip direction are 3° and 14°, respectively. The relatively higher variability observed for dip direction is influenced by the low dip direction value of the K4 joint set (42°), which was measured in various locations. This discrepancy reflects the different survey conditions: field measurements were taken at the base of accessible rock walls, whereas the 3D point cloud interpretation provided access to otherwise unreachable areas, such as vertical walls and upper cliff edges.

The integration of the in situ and remote measurements enabled a comprehensive characterization of the discontinuity systems affecting the rock mass. Table 3.24 summarizes the main characteristics of the joint sets, presenting the averaged attitudes derived from both datasets.

Table 3.24: Characteristics of discontinuity systems derived from field surveys and 3D point cloud photointerpretation.

System	**K1**	**K1a**	**K2a**	**K2b**	**K3**	**K4**
Dip direction / Dip (°)	288/82	124/78	32/79	203/82	227/40	69/30
Aperture (mm)	>5	>5	>5	>5	1–5	1–5
Length (m)	3–10	3–10	1–3	1–3	<1	<1
Spacing (m)	1.2	1.2	<1	<1	0.80	0.50/1
Surface weathering	Slightly weathered	Slightly weathered	Un-weathered	Un-weathered	Slightly weathered	Un-weathered
Filling (type)	Clean	Clean	Clean	Clean	Clean	Soft filling
Roughness	Rough	Rough	Rough	Rough	Rough	Slightly rough
JRC	16–18	16–18	10–12	14–16	10–12	6–8
Humidity	Dry	Dry	Dry	Dry	Dry	Dry
R-value (intact rock)	47	47	49	49	53	54

The collected dataset, deemed satisfactory in both quantitative and qualitative terms, was subsequently employed for the characterization of the rock mass and for the evaluation of potential slope stability phenomena affecting the investigated rock walls.

3.3.4.3 Rock Mass Classification

RMR Method

The basic Rock Mass Rating (RMRb) obtained for the investigated rock mass is 72, which classifies it as a rock mass of "good" quality. According to **Bieniawski (1989)**, several empirical correlations can be applied to estimate key engineering-geological parameters from the RMRb index, namely the friction angle (φ), cohesion (c), and deformation modulus (E). For the present case study, the estimated values are as follows:

$\varphi = 41°$

$c = 0.36\,\text{MPa}$

$E = 44\,\text{GPa}$

Among these parameters, the friction angle was subsequently used as input for the statistical slope kinematic stability analysis, described in Section 3.3.4.4.

Romana Method

The application of the Slope Mass Rating (SMR) method proposed by **Romana (1985)** provided a further characterization of the rock mass. This approach incorporates the RMRb value together with the interaction between discontinuities and slope geometry, which is a fundamental factor for slope stability assessment. The three most common kinematic failure mechanisms—planar, toppling, and wedge failures—were considered.

The SMR analysis was applied to six representative slopes (Figure 3.60).

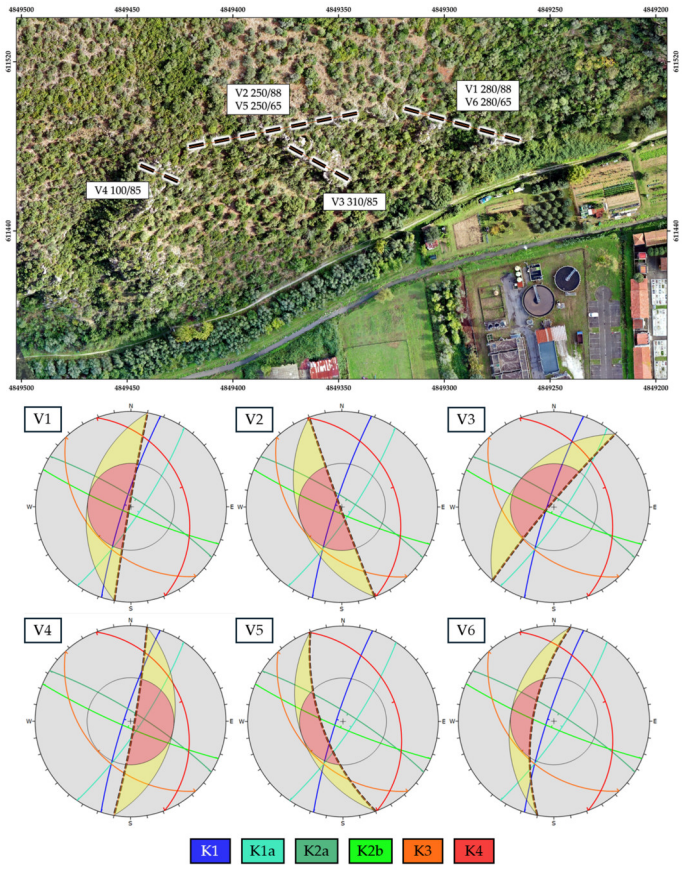

Figure 3.60: Slopes analyzed with the SMR method and subsequent statistical kinematic stability assessment (see Section 3.3.4.4). Stereographic projections (Wulff equal-angle, lower hemisphere) illustrate an example of the kinematic analysis, here represented by a wedge sliding case.

Their dip directions and dip angles were derived from the 3D point cloud interpretation. To account for natural variability in slope orientations, slopes V5 and V6 were also analyzed with a reduced dip angle of 65°, compared to V1 and V2.

Based on the discontinuity sets summarized in Table 3.24 and the six slopes different orientations, SMR values were computed. The results of this analysis are presented in Table 3.25.

Table 3.25: Results of the SMR method application with reference to the six analyzed slopes, as shown in Figure 3.60. (P = planar failure, W = wedge failure, and T = toppling).

Discontinuity System	**V1**			**V2**			**V3**		
	P	W	T	P	W	T	P	W	T
K1 288/82	45*	78	83	80	80	83	67	80	83
K1a 124/78	80	78	77	80	78	83	80	86	66
K2a 32/79	80	78	83	80	78	83	80	78	83
K2b 203/82	80	80	83	80	80	83	80	80	83
K3 227/40	79	81	83	67	86	83	79	79	83
K4 69/30	83	86	86	83	86	81	83	86	86
Discontinuity System	**V4**			**V5**			**V6**		
	P	W	T	P	W	T	P	W	T
K1 288/82	80	81	66	87	80	83	87	83	83
K1a 124/78	67	63	83	87	78	83	87	81	77
K2a 32/79	80	80	83	87	80	83	87	78	83
K2b 203/82	80	80	83	87	67	83	87	62	83
K3 227/40	79	81	83	67	83	87	36*	79	87
K4 69/30	83	86	86	83	86	87	63	86	87

Superscript stars indicate the minimum resulting values.

The obtained results indicate SMR values consistent with a rock mass of "good" (Class II) to "very good" (Class I) quality. Under these conditions, block failures are not expected, and only occasional support measures (e.g., scaling) may rarely be required. The lowest values, equal to 45 (Class III—normal quality) and 36 (Class IV—poor quality), are associated exclusively with planar sliding mechanisms. Specifically, these correspond to the interaction of the K1 (288/82) discontinuity system with slope V1 (280/88) and the K3 (227/40) system with slope V6 (280/65), respectively. In such cases, the rock mass quality falls within the "normal" to "poor" categories, highlighting partially unstable to unstable

slope conditions and the consequent need for stabilization measures and reinforcement interventions.

3.3.4.4 Statistical kinematic stability analysis

The kinematic stability analysis was carried out on the six representative slopes, adopting a rock mass friction angle of $\varphi = 41°$. The results are summarized in Table 3.26.

Table 3.26: Results of the kinematic stability analysis for the six representative slopes. (P = Planar sliding; W = Wedge sliding; DT = Direct toppling; FT = Flexural toppling).

Slope	**Planar Sliding**	**Wedge Sliding**	**Direct Toppling**	**Flexural Toppling**
280/88	K1–K2b–K3	K1/K2b-K1/K2a-K1/K3 (on K3) K1/K1a (on K1) K1a/K3 (on K1a)	K1a/K2a-K1/K1a-K1a/K2b (Oblique Toppling)	–
250/88	K1–K2b–K3	K1/K2b-K1/K3 (on K3) K1/K1a-K1a/K3 (on K1a)	K1a/K2a-K1/K1a-K1a/K2b (Oblique Toppling)	–
310/85	K1–K3	K1/K2a-K1/K2b-K1/K4 (on K1)	K1a/K2b-K2a/K2b-K2a/K4- K2b/K4-K3/K4-K1a/K2a (Oblique Toppling)	K1a
100/85	K1a–K2a	K1a/K2a-K1a/K2b-K1a/K4 (on K1a)	K2b/K3-K1/K2a-K1/K2b (Oblique Toppling)	K1
250/65	K3	K1a/K3 (on K1a) K1/K3-K1/K1a (on K1)	K1a/K2a-K1/K2a-K1a/K2b (Oblique Toppling)	–
280/65	K3	–	K1a/K2a-K2a/K2b-K1a/K2b (Oblique Toppling)	–

3.3.4.5 Multitemporal monitoring through RTS

Before presenting the results of the multitemporal monitoring, it is essential to demonstrate the reliability of the acquired measurements. Table 3.27 reports the average precision values estimated for each RTS monitoring survey. The slope distance precision, expressed in millimeters, ranges between 0.1 and 0.2 mm. The angular precision, expressed in seconds ($''$), varies between 1.1 and 4.2 for the azimuthal angle and between 0.9 and 1.5

for the zenithal angle.

Table 3.27: Summary of the average precision values for each RTS monitoring survey.

RTS Survey	**Slope Distance Precision (±mm)**	**Azimuthal Angle Precision (±″)**	**Zenithal Angle Precision (±″)**
0	0.2	1.8	1.5
1	0.1	2.2	0.9
2	0.2	2.5	1.1
3	0.1	1.6	1.0
4	0.1	3.7	1.3
5	0.1	3.1	1.5
6	0.2	4.2	1.1
7	0.2	4.1	1.1
8	0.1	1.1	1.1

The obtained precision values align well with the uncertainty thresholds previously established for the monitoring prisms (Table 3.22). The outcomes of the multitemporal monitoring survey, which also included the baseline survey (Survey n.0) used as a reference, are presented in two ways. In the first way, the results are displayed through planimetric error ellipses (Figures 3.61 and 3.62). In the second way, the temporal evolution of displacements is represented in diagrams plotting prism IDs against measured values, both in terms of differential slope distance (i.e., the distance from the base station to each prism; Figure 3.63A) and elevation (Figure 3.63B). In these diagrams, the red vertical bars indicate the corresponding slope distance and elevation uncertainty thresholds, whose derivation is described in Section 3.3.3.5.

The analysis of Figures 3.61 and 3.62 does not reveal any systematic pattern of instability, but rather a random distribution of prism displacements. Specifically, prisms B2, B3, B4, B18, B25, B28, B29, and B30 (8 out of 30) consistently remained within their respective error ellipses.

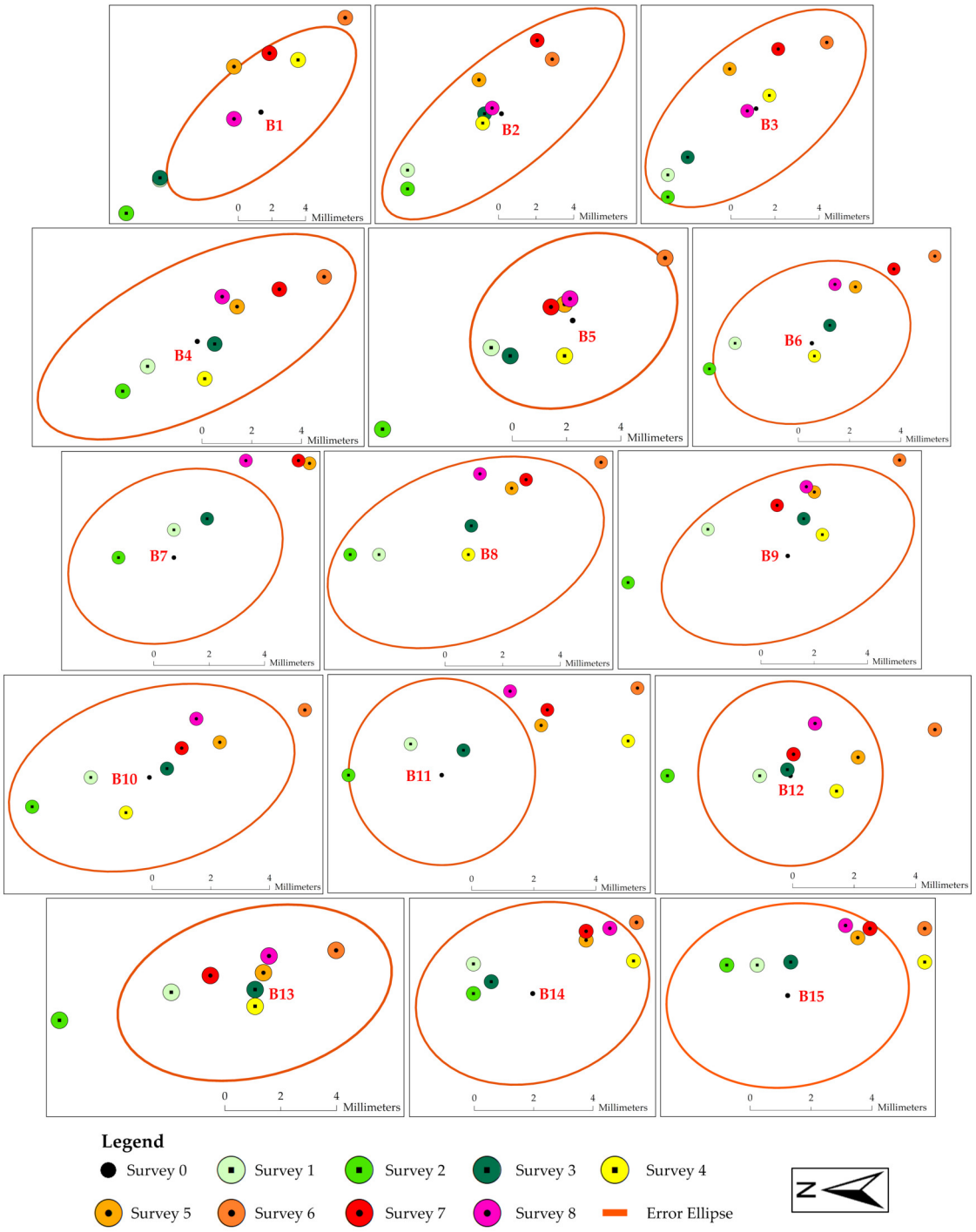

Figure 3.61: Plan view of the multitemporal monitoring results (prisms B1–B15). Orange ellipses represent the error associated with each prism, while colored points indicate the nine survey campaigns.

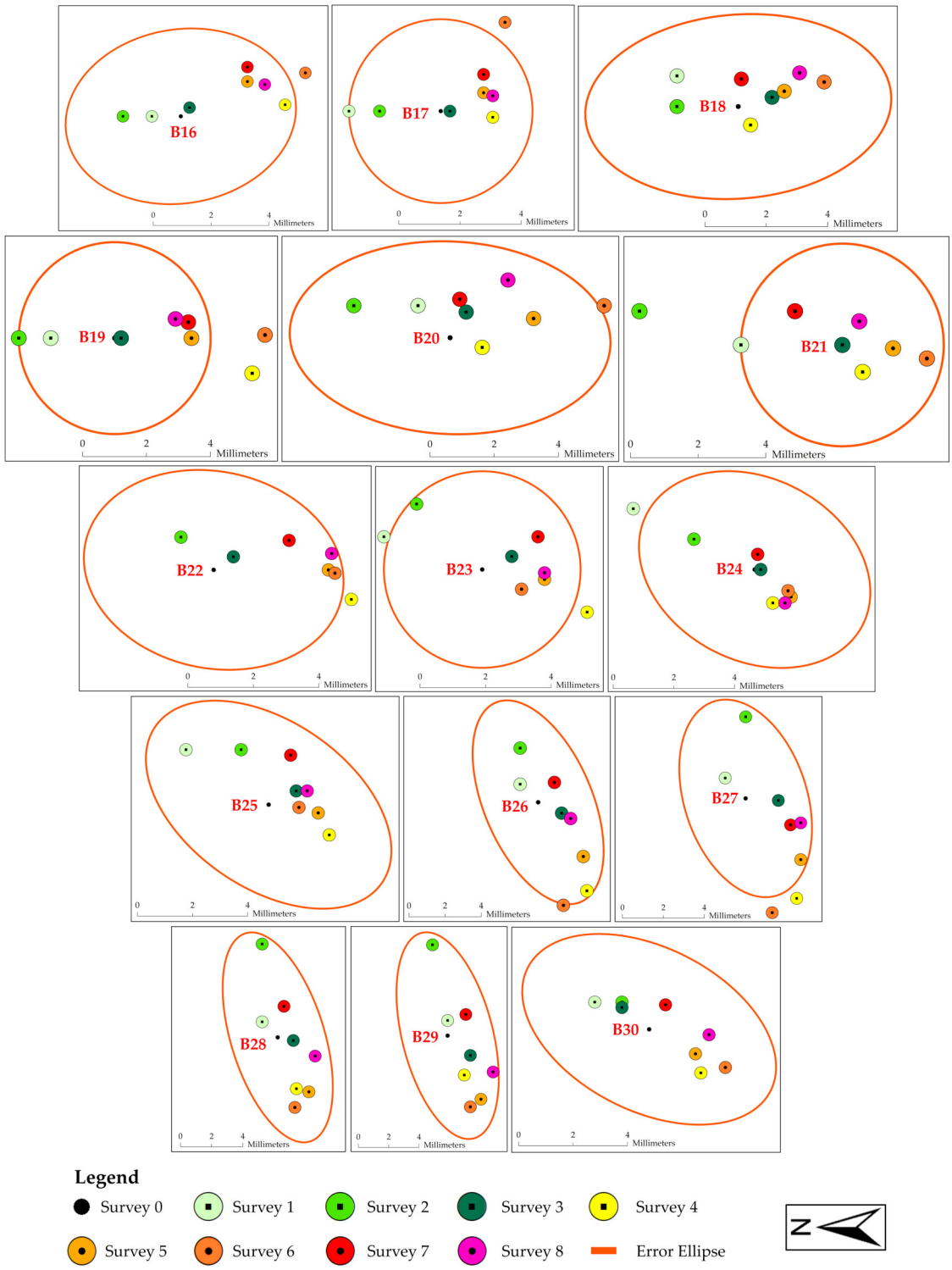

Figure 3.62: Plan view of multitemporal monitoring results for prisms B16–B30. Error ellipses are shown in orange, and colored points correspond to the nine survey campaigns.

The remaining prisms occasionally exceeded the uncertainty ellipses during the monitoring period; however, they were still clearly identifiable by the RTS at the end of the observation interval (December 2021), suggesting overall stability.

In the diagrams presented in Figure 3.63, no clear displacement trends can be identified, with the exception of the last two monitoring sessions—Survey n.7 (12 October 2021, brown) and Survey 8 (13 December 2021, dark grey). For Survey n.7, several prisms show differential slope distances (Figure 3.63A) approaching the uncertainty thresholds, whereas Survey n.8 results fall entirely within tolerance. Conversely, vertical displacements (Figure 3.63B) exceed the threshold in both campaigns.

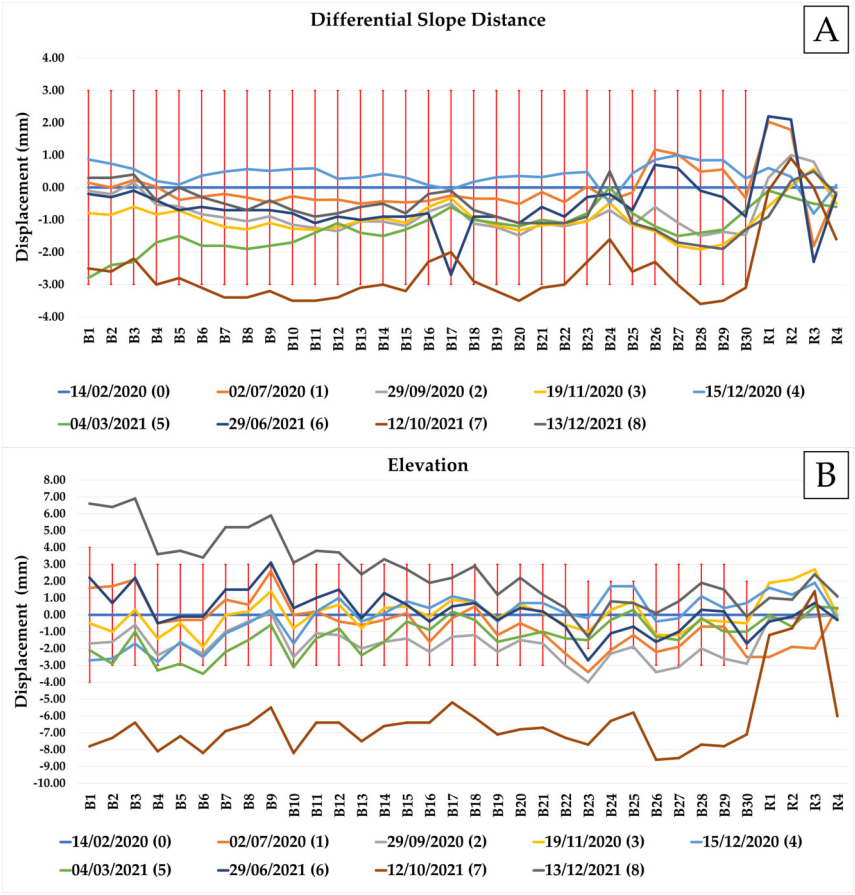

Figure 3.63: Differential slope distance (A) and vertical displacement (B) of prisms measured in all RTS surveys. Red vertical bars mark the uncertainty thresholds for each prism.

The anomalous behavior detected during the seventh survey required additional inves-

tigation: two complementary approaches were adopted: (i) re-evaluation of the reference prisms and RTS station stability, and (ii) verification of potential ground movements using PSI techniques, as described in Section 3.3.3.6.

Data from Survey n.7 indicate coherent vertical shifts among prisms, suggesting that the apparent anomaly may stem from local vertical displacements at the RTS base combined with the multitemporal survey design. To evaluate this, differential distances and elevations were recalculated using prism R4—installed on a stable rocky outcrop—as the sole reference (Figure 3.64).

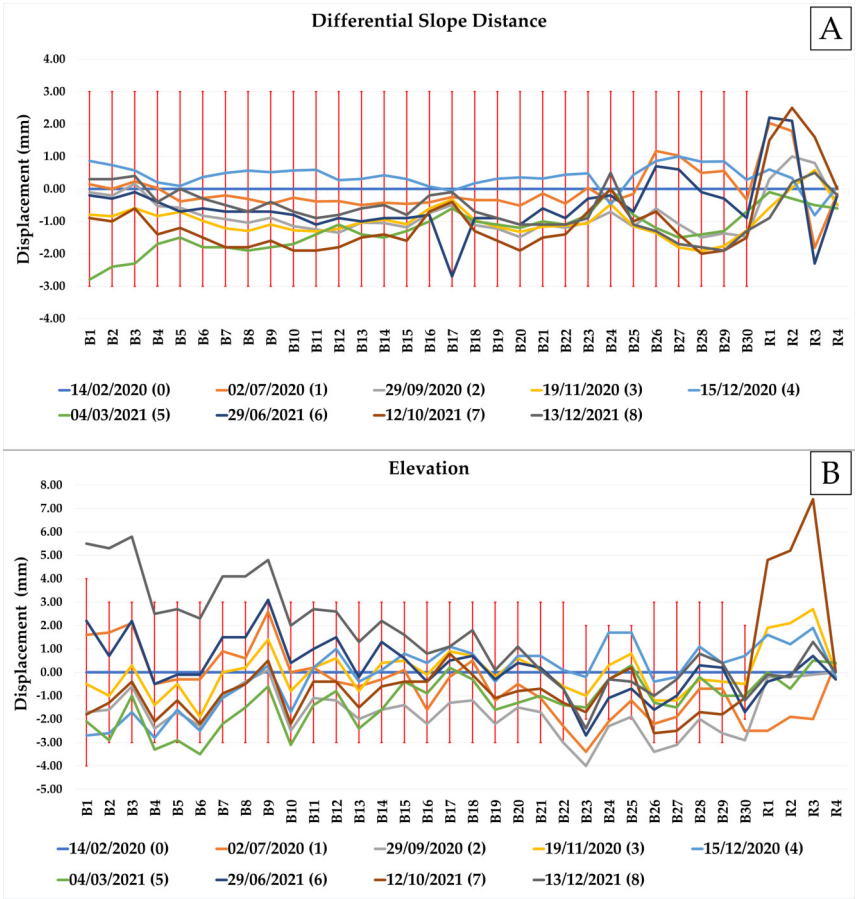

Figure 3.64: Differential slope distance (A) and elevation displacement (B) of each prism as computed with respect to R4. The uncertainty thresholds for each prism are indicated by the red vertical bars.

This choice was motivated by the fact that R1, R2, and R3 are mounted on structures

in the alluvial plain, potentially subject to natural vertical displacements. Moreover, during Survey n.8, some of the more distant prisms recorded vertical deviations close to or beyond instrumental tolerances (e.g., B1–B12 and B14 in Figure 3.63B), which may reflect upward vertical movements.

When recalculated using R4 as the stable reference, results from both surveys demonstrate that slope distances and vertical displacements for all monitoring prisms fall within the defined uncertainty thresholds. Only R1, R2, and R3 exceeded the elevation limits during Survey n.7, while Survey n.8 highlighted minor exceedances for the farthest prisms (B1–B3, B7–B9) and values at the threshold for B4–B6.

To clarify the anomalous behavior of the reference and monitoring prisms that exceeded the tolerance thresholds, a PSI analysis was performed. The outcomes of this analysis are presented in Section 3.3.4.6.

3.3.4.6 Persistent Scatterer Interferometry

The study area poses several challenges for satellite-based PSI analysis due to the coexistence of dense vegetation (trees and shrubs) at slope crests and bases, steep vertical cliffs, and agricultural fields surrounding the RTS installation site. As noted in Section 3.3.3.6, vegetation and croplands reduce PS visibility because of their seasonal variability, often resulting in the absence of stable scatterers. To overcome these limitations, artificial corner reflectors were installed along the upper edges of the rocky escarpments (see Figure 3.55), ensuring the presence of reliable targets.

The results of the PSI analysis are shown in Figure 3.65, with outcomes derived from Sentinel-1A (Figure 3.65A) and Sentinel-1B (Figure 3.65B). Persistent scatterers are color-coded according to their Line of Sight (LOS, from the satellite to the ground) velocity in millimeters per year. The velocity ranges adopted follow standard PSI conventions and are consistent with those employed by the regional interferometric service LaMMa (**LaMMa, 2021**), allowing direct comparison between datasets.

Both PSI datasets show that the alluvial plain where the RTS is located is characterized either by stability (−2.0 to +2.0 mm/year, green scatterers) or slight subsidence (−5.0 to -2.1 mm/year, orange scatterers). These values represent average LOS displacements over the full monitoring interval, from the first to the last available acquisition. Because suitable descending-orbit Sentinel-1 imagery was unavailable for the same time span, vertical and horizontal contributions could not be separated. Nevertheless, the predominance of the negative vertical component suggests that the observed displacements are best interpreted as subsidence. Possible causes include seasonal fluctuations of the groundwater table within unconsolidated alluvial–colluvial deposits, as well as extraction from public and private pumping wells.

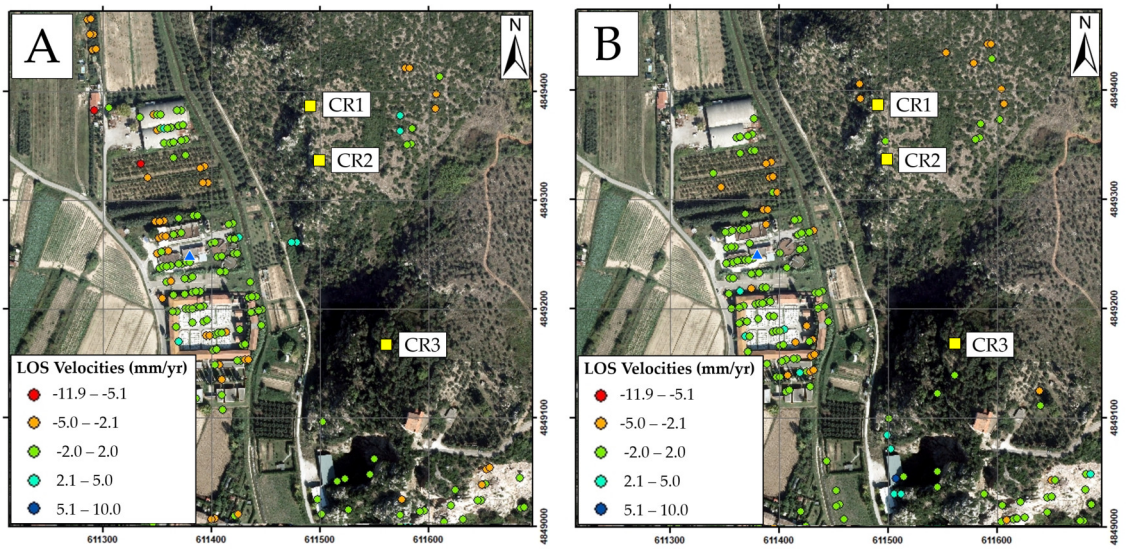

Figure 3.65: PSI results expressed as LOS velocities (mm/yr) for Sentinel-1A (A) and Sentinel-1B (B). Yellow squares mark the artificial corner reflectors installed on the top of the rocky slopes, while the blue triangle indicates the building hosting the RTS.

To validate these findings, results were compared with those published by the regional LaMMa interferometric service for the same imagery and time period (**LaMMa, 2021**). Figure 3.66 shows the PSs identified by LaMMa, including point ID “FV6XKKY,” which is located near the RTS. The accompanying time series depicts its LOS velocity during

the RTS monitoring interval (Survey n.0, February 14, 2020, to Survey n.8, December 13, 2021).

During the seventh RTS survey (October 2021), the PS velocity exhibited a negative trend, indicating moderate subsidence. In contrast, during the eighth survey (December 2021) the velocity turned positive, suggesting slight uplift.

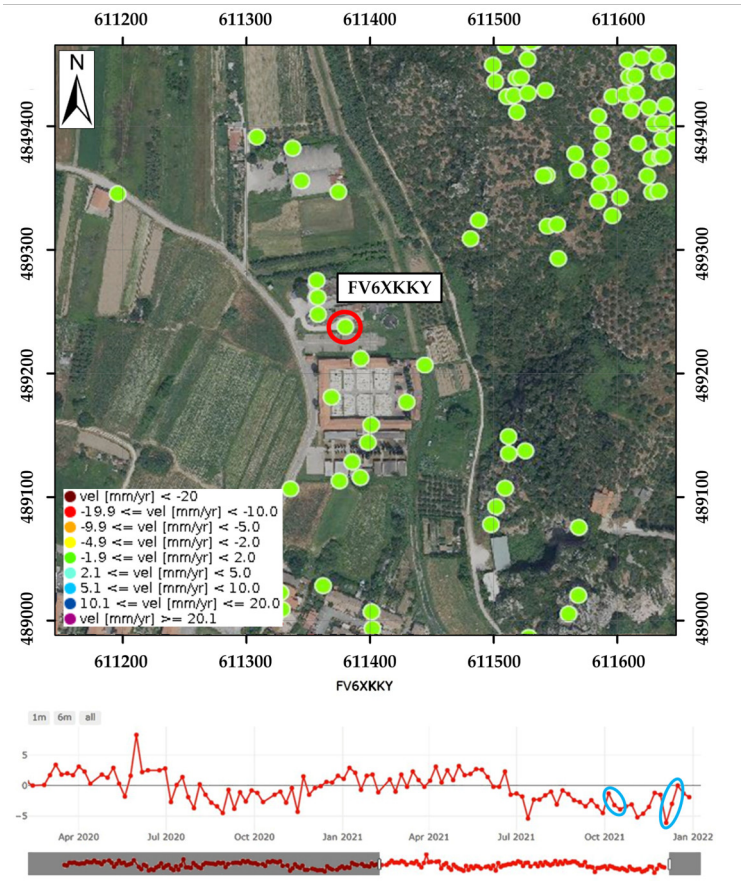

Figure 3.66: PSs detected by the LaMMa regional interferometric service in the study area. The red circle highlights point FV6XKKY near the RTS. The lower diagram displays the LOS velocity trend (mm/yr) for this PS over the RTS monitoring period. Light blue ellipses mark the acquisition dates of the 7th and 8th RTS surveys.

This oscillatory behavior is consistent with seasonal vertical fluctuations of the alluvial plain, likely linked to aquifer dynamics and anthropogenic pumping activity. These interpretations are further supported by the reprocessing of RTS data using the R4 prism

as elevation reference, located on a stable rock outcrop (see Figure 3.64). In this configuration, prisms B1–B30 remained within uncertainty thresholds, whereas the reference prisms R1–R3, situated in the alluvial plain along with the RTS, displayed anomalous displacements—particularly in elevation—confirming the tendency toward subsidence.

The uncertainties associated with the vertical stability of the RTS installation site, as demonstrated by PSI, also explain why several prisms exceeded tolerance thresholds in the eighth RTS survey, particularly those located at greater distances from the instrument. Importantly, no evidence of block falls was recorded during the monitoring period: no new debris was observed at the base of the cliffs, and all prisms remained identifiable by the RTS. The two isolated scatterers visible in light blue in Figure 3.65A, with velocities of 2.1–5.0 mm/year, are not sufficient to be attributed to rockfall deposits.

3.3.5 Discussion

The two-year multitemporal monitoring campaign investigated potential rockfall hazards affecting steep limestone cliffs characterized by karst phenomena. Analysis of the nine RTS measurement campaigns (one initial baseline plus seven monitoring surveys) demonstrates that none of the monitored prisms experienced significant displacements or displayed systematic temporal trends, either in elevation or differential slope distance.

Anomalies emerged only during the seventh campaign, when several prisms recorded irregular vertical movements. These deviations are attributable to ground instability within the Serchio River alluvial plain, where the RTS base and reference prisms R1, R2, and R3 are installed. Minor planimetric deviations, generally within or just above instrumental tolerances, were also observed. The largest variations occurred in prisms located farthest from the instrument, but even these values tended to normalize in subsequent surveys. Such vertical fluctuations are consistent with seasonal aquifer dynamics and the influence of pumping wells.

Overall, the monitoring data support the interpretation of long-term slope stability.

Small inconsistencies can largely be explained by the multitemporal acquisition strategy—since the RTS was reinstalled for each campaign—and by inevitable alignment differences. Although the iron plate and basement ensured leveling, perfect replication of the instrument setup could not be guaranteed. Atmospheric refraction also introduced seasonal and daily oscillations in distance measurements, which are amplified across rugged terrain (elevation differences) or when high-precision EDMs are employed. More reliable corrections would require long-term atmospheric observations and an ad-hoc microclimate model supported by stable reference points (**Artese & Perrelli, 2018**).

Thermal expansion and contraction of the RTS mounting plate, despite its resistant design, may further influence instrument initialization (**Carvill, 1993**). In addition, the short (<100 m) distance between the RTS base and the orientation point R4—imposed by site constraints—makes azimuthal readings sensitive to error, especially for distant prisms. Even small angular inaccuracies can generate apparent displacements; redundancy in observations was therefore systematically adopted to mitigate this effect (**Afeni & Cawood, 2018**). For this reason, the uncertainty thresholds reported in Table 3.221 were applied to all prisms.

Complementary PSI analysis reinforces the evidence of slope stability, with LOS velocities typically falling within the method's tolerance (±2 mm/year) or slightly outside (−5 to +5 mm/year).

The irregular distribution of Persistent Scatterers (PSs) on natural rock walls limits the possibility of obtaining highly reliable monitoring results. To address this limitation, in the present study, three artificial corner reflectors were installed along the upper slope margin, with the purpose of increasing the density of coherent targets and enhancing the precision of displacement measurements (**Ferretti et al., 2007**; **Strozzi et al., 2013**). The detectability of these reflectors in SAR imagery, quantified through the Signal to Clutter Ratio (SCR), is conditioned by several factors—including topographic setting, vegetation

cover, and soil moisture—that need to be evaluated prior to installation (**Czikhardt et al., 2022**; **Garthwaite, 2017**). In this case, their clear visibility was only partially ensured due to multiple concurrent elements, such as the closeness to steep carbonate rock walls of the "Calcare Massiccio" Formation, characterized by high natural reflectivity, the heterogeneous distribution of vegetation (trees and shrubs), and the limitations imposed by image spatial resolution and accuracy. Therefore, only an extended monitoring period, potentially supported by SAR data with finer spatial resolution, would allow a full assessment of their actual visibility and operational effectiveness, which could not be completely validated at the time of this study.

It should be noted that PSI displacements are LOS-based and cannot be decomposed into vertical and horizontal components without additional descending-orbit acquisitions (not available for the analyzed time span due to their unsuitability in terms of spatial correspondence) or independent geodetic data. In this context, precise leveling within the alluvial plain would provide a more direct validation of the subsidence phenomenon (**Cigna et al., 2021**; **Shi et al., 2021**; **Zerbini et al., 2007**).

To corroborate the outcomes of the multitemporal monitoring conducted between February 2020 and December 2021, an additional RTS survey was performed on 4 March 2024, i.e., two and a half years later, under the same instrumental settings and using the same prism configuration. The results of this survey, expressed in terms of differential slope distance and elevation displacements relative to Survey n.0, are illustrated in (Figure 3.67A and 3.67B), respectively. This supplementary dataset provides further confirmation of the stability of both the installed prisms and the monitored rock walls. The plots in Figure 3.67 highlight that prism B3 (monitoring) and prism R3 (reference) were not successfully recorded by the RTS. In the case of R3, no clear explanation could be established, as the prism remains intact, unmoved, and visually detectable from the RTS station. Conversely, the absence of measurements for prism B3 is attributed to the obstruction of the line of sight caused by natural vegetation growth.

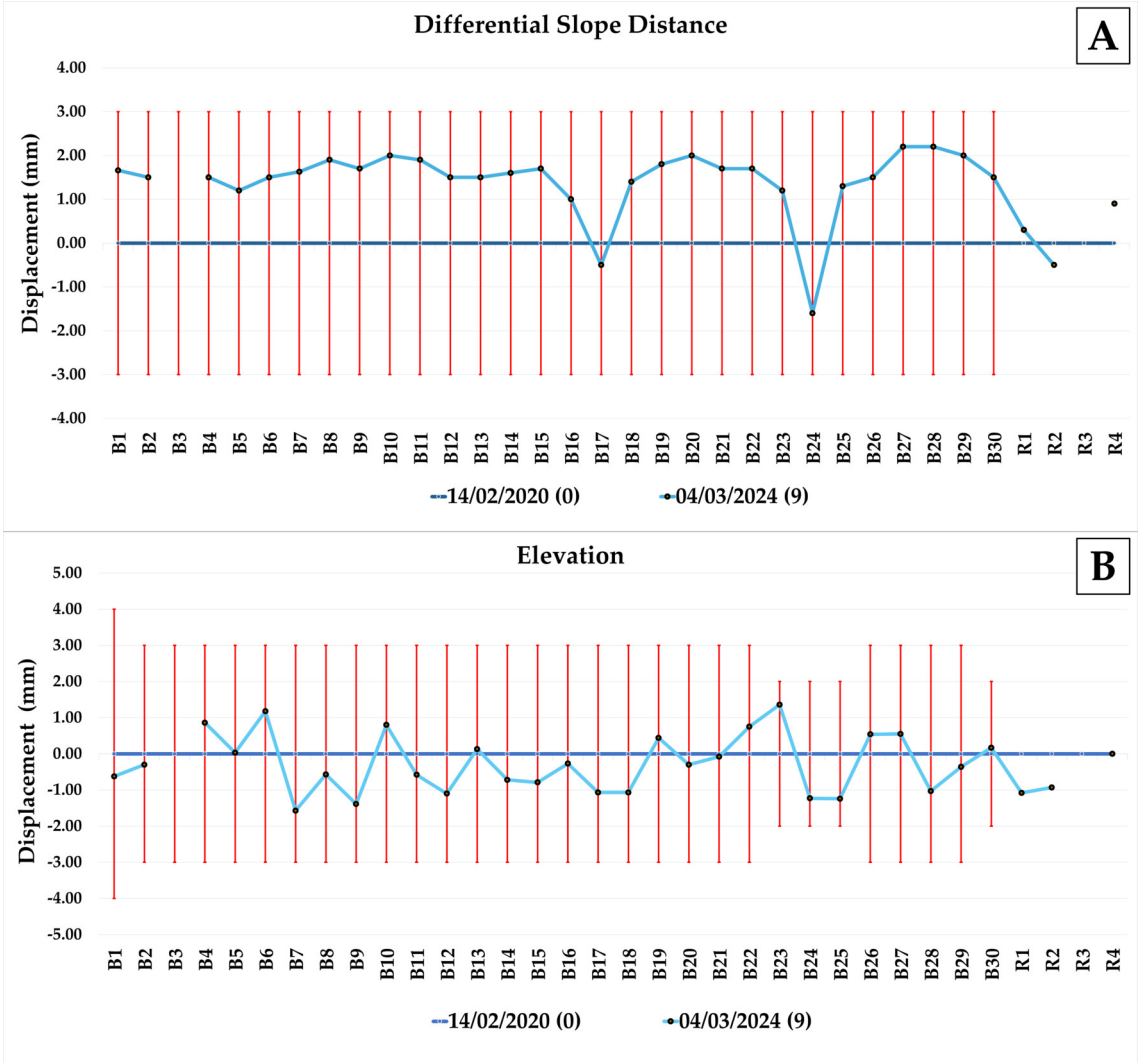

Figure 3.67: Differential slope distance (A) and elevation displacement (B) of each prism as measured during the survey conducted on 4 March 2024.

The application of RTS monitoring at the Vecchiano rock slope presents a balance between high measurement precision and costs. More than continuous monitoring, the adopted method represents a multitemporal survey that, for its own characteristics, may lose precursors of sudden block failures, which can develop over very short timescales or at a scale too localized to be detected by the implemented discrete network. Rockfalls in carbonate formations such as those at Vecchiano are generally characterized by brittle behavior and may occur rapidly once kinematic conditions are satisfied, often with limited

or no detectable precursory displacement.

Moreover, even if RTS provides millimetric accuracy and allows the acquisition of targeted time series on selected blocks identified as potentially unstable, the method requires a stable line of sight and is sensitive to environmental factors, including atmospheric conditions and the stability of the reference system. In the specific case of Vecchiano, the installation of the RTS on the Serchio alluvial plain introduced additional uncertainties related to ground deformation and seasonal aquifer fluctuations, affecting also the reference points.

To overcome these limitations and to allow the monitoring also of points located at the top of the slopes, the integration of RTS with PSI data, as represented in this work, is a valuable approach that allowed distinguishing between slope-related movements and ground deformation affecting the monitoring base. Future developments should include continuous monitoring systems and the integration of geotechnical sensors (e.g., extensometers, pore-pressure sensors) in order to better capture potential early-warning signals in such structurally controlled environments.

Taken together, the findings highlight several limitations: (i) RTS provides high-precision point measurements but lacks full slope coverage; (ii) discrete, multitemporal surveys may overlook transient processes; (iii) repositioning introduces setup-related errors; and (iv) environmental variability can affect accuracy, especially for distant prisms. PSI offered useful complementary information, particularly for slope edges not visible from the RTS, but its performance was constrained in vegetated and morphologically complex terrain.

3.3.6 Conclusions

The combined use of RTS surveys and PSI analysis proved to be an effective and comprehensive strategy for monitoring slope stability in rockfall-prone areas. RTS pro-

vided highly accurate point measurements for specific locations and structures, while PSI complemented these results by supplying frequent, temporally dense observations over wide areas. This synergy enabled the detection of subtle displacements and the characterization of broader ground deformation phenomena such as subsidence and slope-scale movements.

Furthermore, the integration of automation capabilities inherent in both techniques can enhance monitoring efficiency by reducing manual data collection and ensuring greater temporal continuity. When combined with traditional engineering–geological investigations, UAV-based photogrammetry, and stability analyses, the RTS–PSI framework constitutes a holistic monitoring system. Such an approach not only secures precision at the single-point scale but also captures temporal variability and spatially extensive deformation, thereby offering a deeper understanding of the dynamics affecting slopes classified by local authorities as high to very high hazard. The outcomes of this research have already contributed to initiating hazard reduction strategies in the area.

To achieve a successful application, the characteristics of the site and the monitoring objectives must be carefully considered. Optimal deployment requires balancing the point-based precision of RTS with the wide spatial coverage and temporal density of PSI, ensuring that both small-scale and large-scale processes are adequately captured. Ultimately, coupling traditional methods with advanced technologies represents a step forward in geodetic monitoring. This integrative approach fosters more resilient and sustainable management of both natural and built environments through a robust understanding of deformation processes.